

Magnetic properties versus interface density in rigid-exchange-coupled amorphous multilayers with induced uniaxial anisotropy

Cite as: J. Appl. Phys. **133**, 073903 (2023); <https://doi.org/10.1063/5.0137889>

Submitted: 06 December 2022 • Accepted: 02 February 2023 • Published Online: 21 February 2023

 Parul Rani,  Petra E. Jönsson,  Sagar Ghora, et al.



View Online



Export Citation



CrossMark

ARTICLES YOU MAY BE INTERESTED IN

[Sputtered terbium iron garnet films with perpendicular magnetic anisotropy for spintronic applications](#)

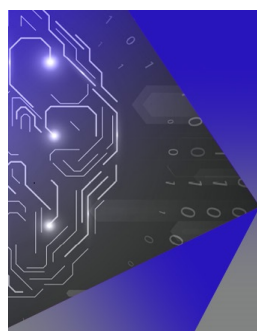
Journal of Applied Physics **133**, 073902 (2023); <https://doi.org/10.1063/5.0139602>

[Measurement of the activation volume in magnetic random access memory](#)

Journal of Applied Physics **133**, 073901 (2023); <https://doi.org/10.1063/5.0135948>

[Toward surface-enhanced Raman scattering using electroless substrate for trace arsenic detection and speciation](#)

Journal of Applied Physics **133**, 073103 (2023); <https://doi.org/10.1063/5.0126372>



APL Machine Learning

Machine Learning for Applied Physics
Applied Physics for Machine Learning

**First Articles
Now Online!**

Magnetic properties versus interface density in rigid-exchange-coupled amorphous multilayers with induced uniaxial anisotropy

Cite as: J. Appl. Phys. 133, 073903 (2023); doi: 10.1063/5.0137889

Submitted: 6 December 2022 · Accepted: 2 February 2023 ·

Published Online: 21 February 2023



Parul Rani,¹ Petra E. Jönsson,¹ Sagar Chorai,² Alpha T. N'Diaye,³ and Gabriella Andersson^{1,a)}

AFFILIATIONS

¹Department of Physics and Astronomy, Uppsala University, Box 516, SE-751 20 Uppsala, Sweden

²Department of Materials Science and Engineering, Uppsala University, Box 35, SE-751 03 Uppsala, Sweden

³Advanced Light Source, Lawrence Berkeley National Laboratory, 1 Cyclotron Road, Berkeley, California 94720, USA

^{a)}Author to whom correspondence should be addressed: gabriella.andersson@physics.uu.se

ABSTRACT

We demonstrate the possibility to tune the saturation magnetization, coercivity, and uniaxial in-plane anisotropy constant in amorphous bilayers and multilayers of $\text{Co}_{85}(\text{Al}_{70}\text{Zr}_{30})_{15}$ and $\text{Sm}_{11}\text{Co}_{82}\text{Ti}_7$ through the interface density. From magnetometry and x-ray circular dichroism (XMCD) measurements, we conclude that the easy-axis coercivity $\mu_0 H_c$ increases four times when the number of bilayer repetitions, N , increases from 1 to 10 within a constant total sample thickness of 20 nm. At the same time, the anisotropy constant K_u also increases by a factor four, whereas the saturation magnetization M_s decreases slightly. The Co spin and orbital moments, m_s and m_l , are found to be approximately constant within the sample series. The average total Co moment is only 0.8–0.9 μ_B /atom, but the m_l/m_s ratio is strongly enhanced compared to pure Co. Magnetization curves extracted from XMCD measurements show that the Co and Sm moments are ferromagnetically coupled for all samples.

© 2023 Author(s). All article content, except where otherwise noted, is licensed under a Creative Commons Attribution (CC BY) license (<http://creativecommons.org/licenses/by/4.0/>). <https://doi.org/10.1063/5.0137889>

I. INTRODUCTION

Magnetic thin film heterostructures, multilayers, or superlattices are presently frequently incorporated in information storage and spintronic devices.^{1,2} Layered structures with magnetically hard and soft phases, where the hard phase contributes to the coercivity and the soft phase gives high saturation magnetization, are artificial magnetic materials with different properties compared to single-phase materials.^{3–8} The magnetic properties of such soft/hard structures depend strongly on the layer thicknesses. If the soft layers are thin enough, typically some tens of nanometers, all magnetic moments in the soft phase will follow the hard-phase magnetization direction strictly, i.e., the system exhibits rigid exchange coupling across the soft/hard interface. Above a critical soft layer thickness, the sample will instead behave as an exchange spring system, where the soft layer moments change their orientation reversibly in an applied field.

With amorphous layers, it is possible to achieve high uniformity and well-defined interfaces without lattice strain, atomic steps,

or other types of structural defects, in combination with magnetic properties that can be tuned to a large extent through composition.^{9–11} The possible combinations of soft and hard amorphous magnetic materials are, therefore, almost unlimited. In amorphous structures, it is furthermore possible to significantly alter the microscopic magnetic properties through sample design and growth conditions, e.g., introducing imprinted uniaxial anisotropy, or a certain amount of intermixing at the interfaces.^{9,12–14}

In the present study, we examine the magnetic properties of a model system of rigid-exchange-coupled amorphous heterostructures, both bilayers and multilayers, with $\text{Sm}_{11}\text{Co}_{82}\text{Ti}_7$ (denoted SmCoTi) as the hard phase and $\text{Co}_{85}(\text{Al}_{70}\text{Zr}_{30})_{15}$ (denoted CoAlZr) as the soft phase.^{14,15} A uniaxial in-plane anisotropy has been imprinted in the samples by applying an external magnetic field during growth. The focus is on room-temperature magnetic properties (saturation magnetization, coercivity, anisotropy energy, and Co magnetic moments), and how these are affected by the interface density. Equal individual layer thickness of two phases is chosen in

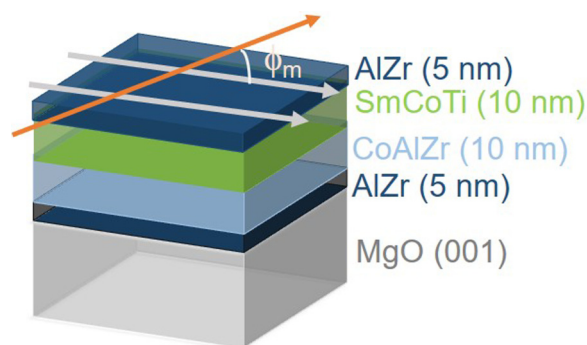


FIG. 1. Schematic representation of a $[\text{SmCoTi}(10\text{ nm})/\text{CoAlZr}(10\text{ nm})] \times 1$ sample grown on MgO (001). The hard magnetic phase SmCoTi is shown in green, the soft magnetic phase CoAlZr is shown in light blue, and the AlZr buffer and cap layers are dark blue. White arrows indicate the direction of the in-plane magnetic field applied during growth, parallel to one substrate edge. The in-plane measurement angle ϕ_m , used in magnetization and XMCD measurements, is defined with respect to this axis.

order to keep the average composition fixed within the sample series.

II. EXPERIMENTAL DETAILS

Amorphous CoAlZr-SmCoTi multilayer samples were prepared by DC magnetron co-sputtering from Sm, Co, Ti, and $\text{Al}_{70}\text{Zr}_{30}$ targets onto $10 \times 10\text{ mm}^2$ MgO (001) substrates at room temperature. Prior to sputtering, the vacuum chamber was evacuated to a base pressure below $\sim 10^{-10}$ Torr, and during sputtering,

the argon pressure was 2.0×10^{-3} Torr. The sample holder was rotated at 20 rpm for a homogeneous growth, with respect to both thickness and composition. To imprint a uniaxial magnetic anisotropy in the magnetic layers, an in-plane magnetic field of magnitude 130 mT was created using permanent magnets fixed into the substrate holder.^{10,11,13}

$\text{Co}_{85}(\text{Al}_{70}\text{Zr}_{30})_{15}$ and $\text{Sm}_{11}\text{Co}_{82}\text{Ti}_7$ were deposited in an alternating multilayer structure with nominal individual layer thickness $t = 10, 2,$ and 1 nm and the number of repetitions was correspondingly $N = 1, 5,$ and 10 to achieve a similar total thickness of 20 nm of the magnetic part of each sample. To avoid creation of crystallites in the magnetic layers, all the samples had a 5 nm $\text{Al}_{70}\text{Zr}_{30}$ amorphous buffer layer on the substrate.¹⁰ A final protective cap layer to prevent oxidation also consisted of 5 nm of amorphous $\text{Al}_{70}\text{Zr}_{30}$ (denoted AlZr). Figure 1 shows a schematic illustration of a sample with $t = 10\text{ nm}, N = 1$, i.e., effectively a bilayer.

To determine the layer thicknesses, densities, interface roughness, and structural quality of the samples, x-ray reflectivity (XRR) and grazing incidence x-ray diffraction (GIXRD) measurements were performed using a Bruker D8 diffractometer with Cu K_α radiation ($\lambda = 1.54\text{ \AA}$). For XRR (using $\theta - 2\theta$ scans), the detector angle range was $0.2^\circ - 6^\circ$, whereas in GIXRD measurements, the grazing incidence angle was fixed at 1° and the 2θ range was $10^\circ - 80^\circ$.

Magnetic hysteresis loops were measured at room temperature using two techniques: (i) Longitudinal magneto-optic Kerr effect (L-MOKE) in a home-built setup, with a maximum field of 0.5 T and the possibility to rotate the sample, thereby applying the magnetic field at different in-plane angles ϕ_m with respect to the growth field direction (parallel to one of the sample edges as illustrated in Fig. 1); (ii) SQUID magnetometry (superconducting quantum interference device, Quantum Design MPMS XL), with the field in the $\phi_m = 0^\circ$ direction.

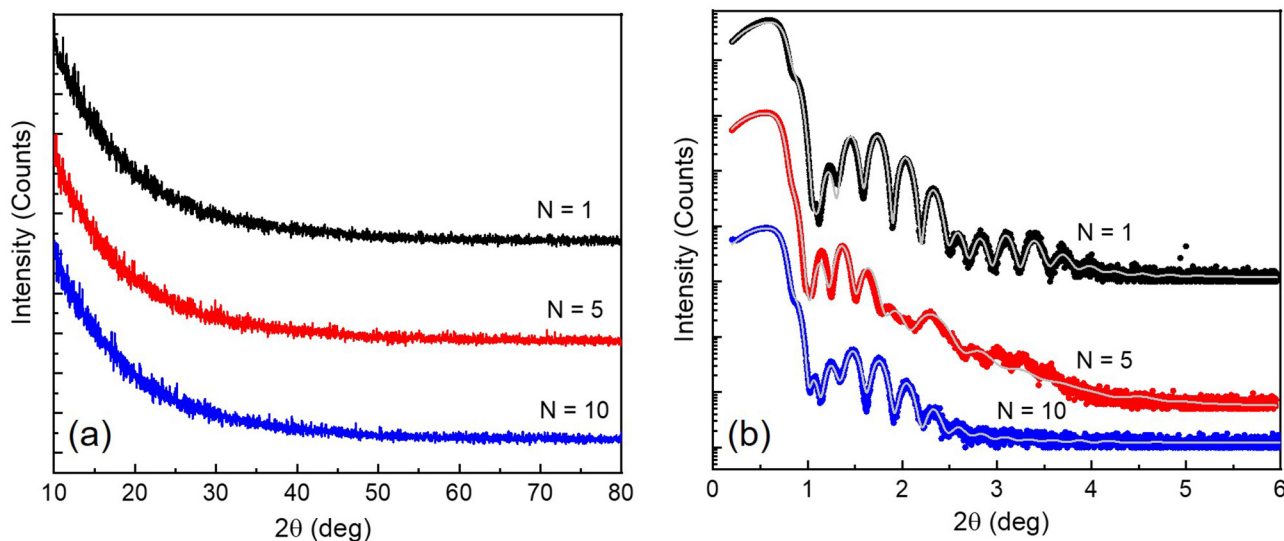


FIG. 2. (a) GIXRD measurements on three different samples. (b) Corresponding XRR data (dots) with GenX reflectivity fits (lines). The data in both panels are offset for clarity.

TABLE I. Individual layer thickness t and the corresponding interface widths σ of all layers in all three samples, extracted from the *GenX*¹⁸ fits of the XRR data shown in Fig. 2. The origin of the interface widths can be both roughness and intermixing. The number densities of CoAlZr and SmCoTi are estimated, from the fits of the individual layer, to be 0.086(1) and 0.078(1) at./Å³, respectively.

Layer	Multilayer (10-10 nm) × 1		Multilayer (2-2 nm) × 5		Multilayer (1-1 nm) × 10	
	t (nm)	σ (nm)	t (nm)	σ (nm)	t (nm)	σ (nm)
Al ₂ O ₃	1.2(5)	0.6(5)	1.6(5)	0.2(5)	0.9(5)	0.6(5)
Al ₇₀ Zr ₃₀ capping	4.3(5)	0.7(5)	4.7(5)	0.1(5)	4.2(5)	0.2(5)
Sm ₁₁ Co ₈₂ Ti ₇	9.8(5)	0.6(5)	1.9(5)	0.7(5)	1.0(5)	1.1(5)
Co ₈₅ (Al ₇₀ Zr ₃₀) ₁₅	10.3(5)	0.4(5)	2.2(5)	0.5(5)	1.0(5)	0.5(5)
Al ₇₀ Zr ₃₀ buffer	5.5(5)	0.4(5)	5.2(5)	0.2(5)	4.0(5)	0.9(5)

X-ray absorption spectroscopy (XAS) and x-ray magnetic circular dichroism (XMCD) measurements were carried out at beamline 6.3.1 of the Advanced Light Source (ALS), Berkeley, to extract element-specific magnetic characteristics of Co and Sm. Luminescence yield (LY) mode was used to monitor x-ray absorption, since this mode makes it possible to probe the entire sample thickness, contrary to the surface-sensitive total electron yield mode more commonly used for XMCD. LY works well for films grown on MgO substrates.¹⁶ XMCD spectra were recorded with fixed x-ray helicity while switching the applied magnetic field between +0.5 and -0.5 T. The field direction was collinear with both the sample edge defining $\phi_m = 0^\circ$ and with the x-ray beam, which impinged on the sample at 60° from the surface normal. Energy ranges were across the Co $L_{3,2}$ edges ($2p \rightarrow 3d$ transitions) as well as the Sm $M_{5,4}$ edges ($3d \rightarrow 4f$ transitions). The 0.5 T field along the easy axis ensured that the samples were saturated. Measurements across the Ti $L_{3,2}$ edges showed no difference between the two field directions, i.e., the Ti atoms remain non-magnetic. Element-specific magnetization loops were also recorded along the easy axis for Co and Sm, with fields up to 0.5 T and the photon energy fixed at an XMCD maximum or minimum to optimize the magnetic contrast for the element of interest.¹⁷

III. STRUCTURAL PROPERTIES

The data from GIXRD and XRR, including reflectivity fits using *GenX*,¹⁸ are shown in Fig. 2. In GIXRD, no Bragg peaks are observed, which confirms that all samples are x-ray amorphous, with only short-range atomic order. In XRR, clear Kiessig fringes are seen up to $2\theta \approx 4^\circ$ for $N = 1$ and $N = 5$ samples and up to $2\theta \approx 3^\circ$ for $N = 10$, indicating a well-defined total thickness. Values for the individual layer thicknesses t and the root-mean-square interface widths σ obtained from *GenX* fits are given in Table I. In the fitting model, σ represents variations in the position of the top of each layer. Therefore, a continuous but wavy layer, with uniform t , can give a similar σ value as a rough layer with thickness variations. We conclude from the XRR data, particularly the Kiessig fringes, that the layers are continuous in all samples, even though the $N = 10$ sample has σ values that are comparable to t for the magnetic layers. The buffer layer interface width is larger for $N = 10$ than for $N = 1$ and $N = 5$, and this is at least partially propagated through the multilayer stack and contributes to the slightly less well-defined total thickness. In all samples, the t values obtained agree well with the nominal layer thicknesses.

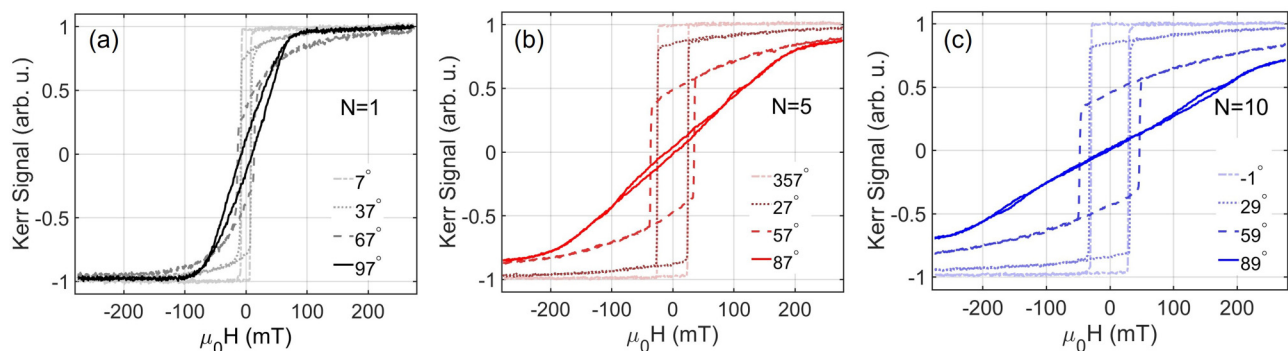


FIG. 3. Normalized Kerr signal vs applied field for (a) multilayer (10-10 nm) × 1, (b) multilayer (2-2 nm) × 5, and (c) multilayer (1-1 nm) × 10, measured at the corrected in-plane angles ϕ coming closest to 0° , 30° , 60° , and 90° , with the easy axis defined as $\phi = 0^\circ$. These were selected to show the main trends in the change of loop shape with varying azimuthal angles.

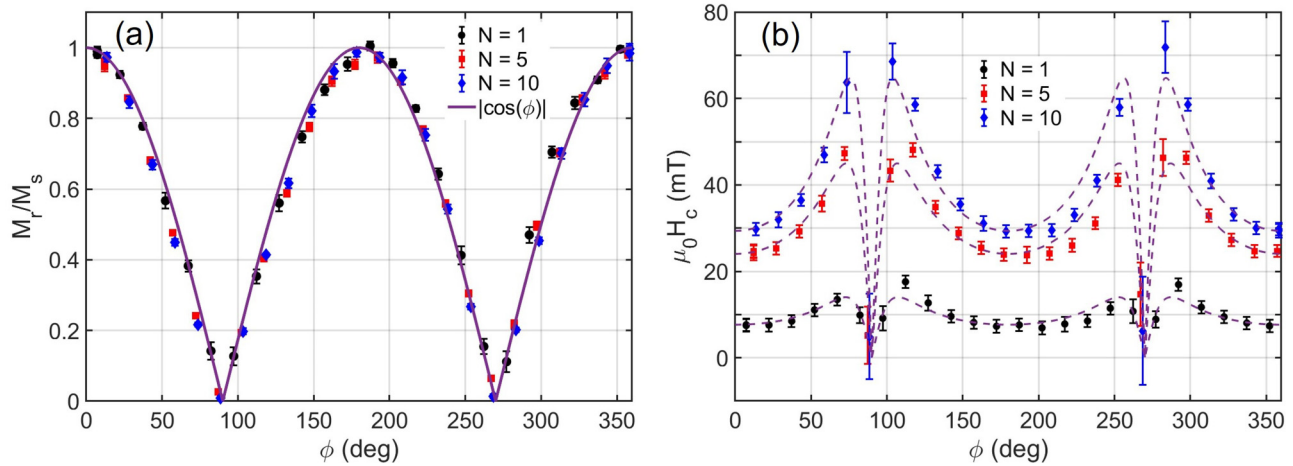


FIG. 4. (a) Data points showing the normalized remanence M_r/M_s vs corrected angle ϕ for the $(10\text{-}10\text{ nm})\times 1$, $(2\text{-}2\text{ nm})\times 5$ and $(1\text{-}1\text{ nm})\times 10$ multilayers, as obtained from L-MOKE $M(H)$ measurements recorded at every 15° . The solid line is the fit to $|\cos \phi|$, where the use of corrected ϕ values brings the easy axis to 0° for all samples, to facilitate comparison. (b) The coercivity $\mu_0 H_c$ vs corrected angle ϕ for the same samples as in (a); dotted lines representing the fits using Eq. (1). The values of $\mu_0 H_c(0)$ obtained in the fits are 8, 24, and 29 mT for the $N = 1, 5$, and 10 samples, respectively. The corresponding values of n are 0.08, 0.08, and 0.05.

IV. MAGNETIC ANISOTROPY

In-plane magnetic hysteresis loops were recorded using L-MOKE with the field applied along different azimuthal measurement angles $\phi_m = 0^\circ - 360^\circ$ in steps of 15° . As indicated in Fig. 1, the angle is defined with respect to the growth field. Saturation was not completely achieved for all angles. We, therefore, used the assumption of approach to saturation,¹⁹ $M = M_s - a/H - b/H^2$, and fitted for simplicity omitting the b/H^2 term, which has its origin in magnetocrystalline anisotropy, to obtain normalized magnetization for all angles. Selected examples of normalized loops are shown in Fig. 3. For all samples, the growth field has imprinted an in-plane anisotropy.

Based on the Stoner–Wohlfarth model,²⁰ the normalized remanence M_r/M_s vs ϕ_m data were then fitted by $|\cos(\phi_m - \alpha)|$, which is applicable to a magnetic material with uniaxial anisotropy. The offset angle α , on the order of a few degrees, is introduced in the fit due to the uncertainty inherent in the alignment of each sample: (i) with respect to the growth field on the deposition chamber sample holder and (ii) in the MOKE measurement. Finally, the corrected angle ϕ was introduced so that M_r/M_s has its maximum value at $\phi = 0^\circ$, for all samples. The resulting data points are shown together with the $|\cos(\phi)|$ fit in Fig. 4(a), verifying the nearly perfect uniaxial anisotropy.

The angular dependence of the coercivity $H_c(\phi)$ is shown in Fig. 4(b). It deviates significantly from the Stoner–Wohlfarth model and is instead fitted to a modified Kondorsky relation obtained considering a two-phase model,^{21–23}

$$\mu_0 H_c(\phi) = \mu_0 H_c(0) \frac{|\cos(\phi)|}{n \sin^2(\phi) + \cos^2(\phi)}, \quad (1)$$

accounting for magnetization reversal processes in multidomain

crystals. Here, n is a factor taking into account demagnetization and uniaxial anisotropy. This relation provides reasonably good fits for all samples, indicating that the field-induced anisotropy direction is well defined.

The saturation magnetization M_s values reported in Table II were determined from the room temperature SQUID hysteresis loops along the in-plane easy axis after subtraction of the diamagnetic contribution from the MgO substrate. The saturation magnetization of the $N = 10$ sample, with wider interfaces, is decreased slightly compared to other two samples. Table II also displays the average moment per magnetic atom, m_{avg} , obtained from M_s values.

For a quantitative estimate of the uniaxial magnetic anisotropy constant K_u , we determined the saturation field H_{sat} by assuming a linear slope of the M/M_s vs H hard-axis MOKE data. The exact approach to saturation is, therefore, not included in this estimate. Then, the approximate formula $K_u = (\mu_0 H_{\text{sat}} M_s)/2$ was used, and $\mu_0 H_{\text{sat}}$ and K_u values are reported in Table II. The anisotropy constant increases considerably from the $N = 1$ sample to the other two. It should be noted that the increase in the saturation field between

TABLE II. Saturation magnetization M_s from SQUID measurements, saturation field $\mu_0 H_{\text{sat}}$ from MOKE hard-axis loops, and the derived anisotropy constant K_u . The average moment per magnetic atom, m_{avg} , was derived from M_s and the number densities obtained from XRR fits.

Sample	M_s (kA/m)	$\mu_0 H_{\text{sat}}$ (mT)	K_u (kJ/m ³)	m_{avg} (μ_B/atom)
$N = 1$	615(62)	74(9)	23(4)	0.91(9)
$N = 5$	630(60)	236(11)	74(8)	0.93(9)
$N = 10$	503(54)	375(12)	94(11)	0.74(8)

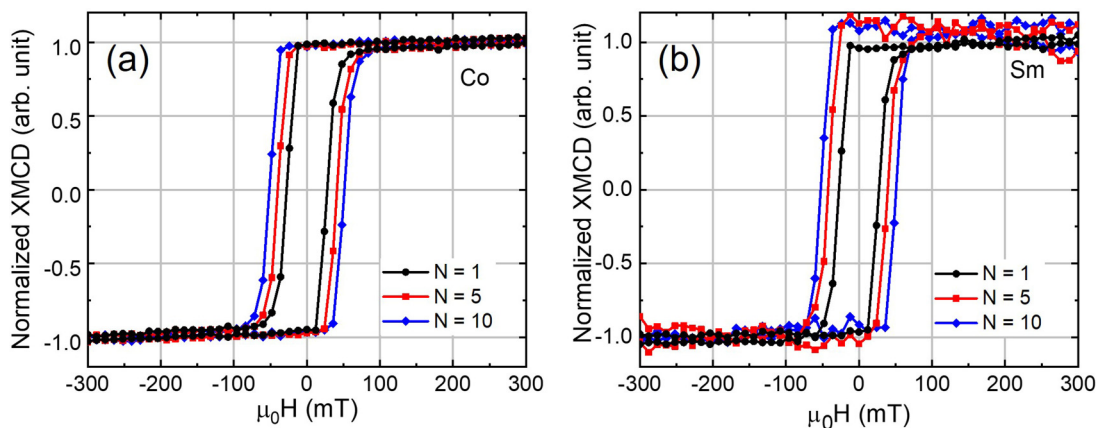


FIG. 5. Normalized element-specific easy-axis hysteresis loops for (a) Co and (b) Sm. The loops were recorded at room temperature, at a measurement angle $\phi_m = 0^\circ$.

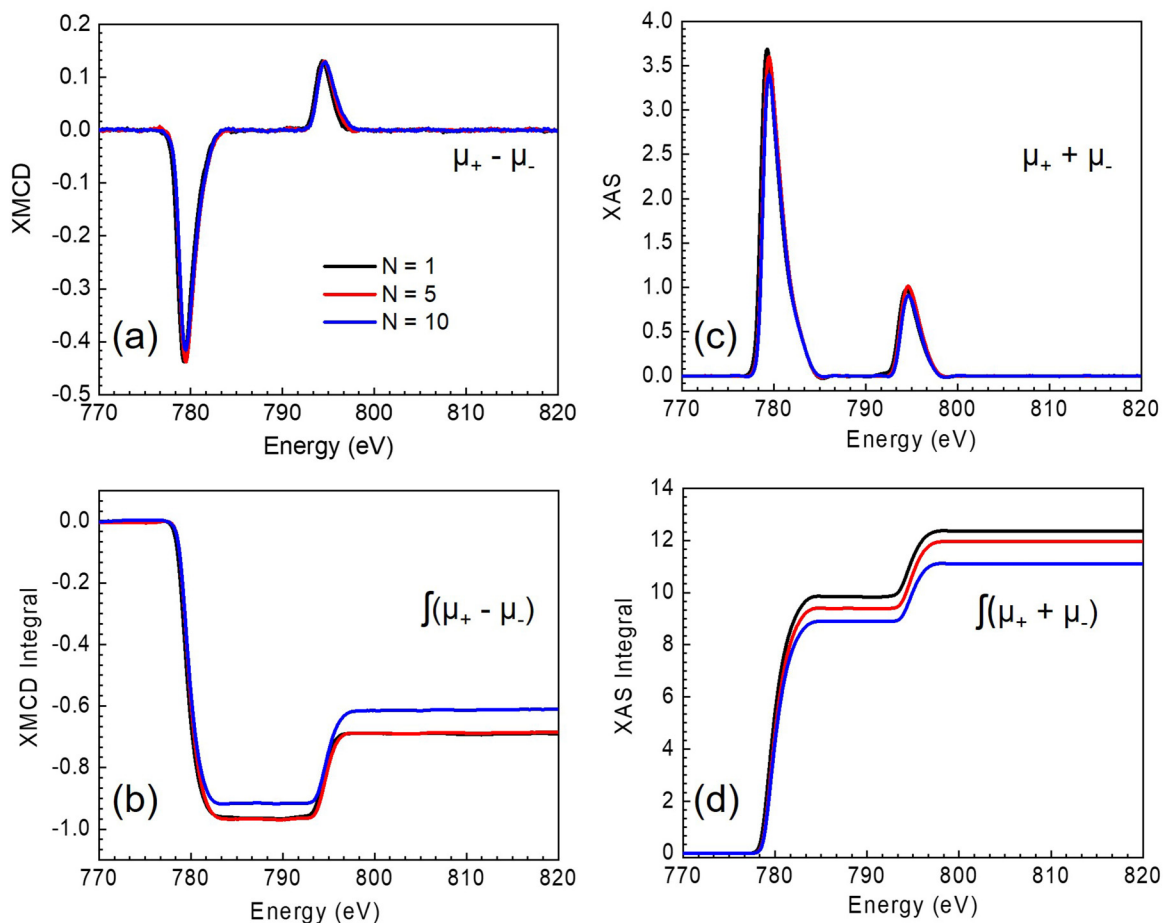


FIG. 6. Background-corrected Co *L*-edge XMCD (a) and XAS (c) of the three CoAlZr/SmCoTi multilayers when saturated in the easy axis direction. Panels (b) and (d) show the integrals of (a) and (c), respectively, which are used for extracting the Co spin and orbital moments. The notation μ_+ and μ_- is explained in the text.

TABLE III. Cobalt spin, orbital, and total magnetic moments (m_s , m_l , and $m_l + m_s$) for all samples as well as the ratio m_l/m_s . The values were obtained at room temperature. Values for Co in CoFeB²⁷ and bulk hcp Co^{17,26} are included for comparison.

Sample	m_l (μ_B/at)	m_s (μ_B/at)	$m_l + m_s$ (μ_B/at)	m_l/m_s
Bulk hcp Co ^{17,26}	0.15(5)	1.55(5)	1.70(7)	0.10
Co in 2 nm CoFeB ²⁷	0.17(2)	0.90(4)	1.07(5)	0.19(3)
Co in 0.85 nm CoFeB ²⁷	0.16(1)	0.57(5)	0.73(5)	0.28(3)
$N = 1$	0.19(1)	0.61(3)	0.80(4)	0.306(3)
$N = 5$	0.19(1)	0.64(3)	0.83(4)	0.301(5)
$N = 10$	0.18(2)	0.69(3)	0.87(4)	0.269(4)

$N = 5$ and $N = 10$ is partially compensated by the decrease in M_s , when combining them into K_u .

V. MAGNETIC MOMENTS

Element-specific magnetic hysteresis loops along the growth field direction, acquired with the photon energy set to L_3 and M_5 absorption edges of Co and Sm, respectively, are shown in Fig. 5. The $M(H)$ loops are close to rectangular, as in the MOKE data for $\phi_m \approx 0^\circ$, and also confirm that the Co and Sm magnetic moments are ferromagnetically coupled.² The coercivity values are higher than those seen in Fig. 3 by a consistent offset of around 20 mT, which is most probably due to a higher remanence in the beamline external magnet than in the L-MOKE setup, which has a Hall probe directly monitoring the field during data collection. Another possible contribution to the observed difference in $\mu_0 H_c(0)$ is that L-MOKE and XMCD do not probe equivalent sample volumes. However, the trends and orders of magnitude in coercivity values are similar for both methods, and we base our analysis in the preceding section on the more precise L-MOKE field values.

Cobalt spin and orbital moments, m_s and m_l , were extracted from the XMCD data using the sum rules.^{24–26} Figure 6(a) shows the background-corrected XMCD signal, $\mu_+ - \mu_-$, for all three samples, and Fig. 6(c) shows the corresponding total x-ray absorption $\mu_+ + \mu_-$. The absorption coefficient is $\mu_+(\mu_-)$ for parallel (antiparallel) alignment of the applied magnetic field and the photon helicity. The sum rule expressions for transition metal m_s and m_l values include the number of $3d$ holes, n_h , as a factor. We have used the value $n_h = 2.5(1)$ for Co based on the previously well-established $n_h = 2.49$ obtained from first-principles calculations,^{17,26,27} and the typical range $n_h = 2.4 - 2.6$ found for Co, with only small variations due to composition, degree of disorder, and local environment.^{28,29} The resulting m_l and m_s values are shown in Table III together with values reported for Co in other systems. The uncertainties given for our data include purely statistical uncertainties and the contribution from the choice of n_h but not any possible systematic errors in the experiment. The ratio m_l/m_s is independent of the assumed number of holes.

We have made an attempt to calculate the Sm moment, m_{Sm} , based on the average magnetic moment per magnetic atom, the Co moment from XMCD, and the layer thicknesses and nominal compositions, reported in Tables I–III. However, the estimated

uncertainties on these Sm moments are of the same order of magnitude as the values themselves. For $N = 1$ and $N = 5$, the derived m_{Sm} values are positive, within the uncertainties, which is also clearly supported by our XMCD data. Using the somewhat decreased saturation magnetization for the $N = 10$ sample, m_{Sm} can still be positive, but it is considerably smaller. It should be noted that all three samples have similar XMCD signatures for Sm, i.e., m_{Sm} should not change sign. Previous studies of Sm–Al compounds^{30–32} have indicated that the Sm moment can be strongly affected by composition variations, and that m_{Sm} can even be zero due to antiparallel alignment of spin and orbital moments. It, therefore, seems quite likely that the decrease in saturation magnetization for $N = 10$ is related to lower Sm moments due to the roughness/intermixing in the interface regions.

VI. CONCLUSIONS

We have investigated the influence of interface density on the magnetization reversal and Co moments of amorphous CoAlZr/SmCoTi multilayers with imprinted uniaxial in-plane anisotropy. It is found that soft and hard layers are rigidly coupled across the interfaces and that both the coercivity and the anisotropy constant increase significantly by a factor of approximately 4, with an increased number of bilayer repetitions within the constant total sample thickness. The imprinted uniaxial in-plane anisotropy is confirmed by characteristic angular dependence of both remanence and coercivity, which indicate a well-defined preferred direction. Our study clearly demonstrates the possibility to tune coercivity and anisotropy constants in amorphous Co-based hard/soft multilayers through the interface density, while maintaining a reasonably high saturation magnetization. This is of interest for, e.g., magnetic devices based on such nanostructures. The possibility to imprint a perpendicular anisotropy axis with an out-of-plane growth field should be explored in the future.

ACKNOWLEDGMENTS

Financial support from the Swedish Research Council (G.A.; Project Grant No. 2017-03725) and from the Swedish Foundation for Strategic Research (S.G.; SSF Contract No. EM-16-0039) is gratefully acknowledged. This research used resources of the Advanced Light Source, a U.S. DOE Office of Science User Facility under Contract No. DE-AC02-05CH11231.

AUTHOR DECLARATIONS

Conflict of Interest

The authors have no conflicts to disclose.

Author Contributions

Parul Rani: Conceptualization (lead); Data curation (equal); Formal analysis (equal); Investigation (lead); Visualization (equal); Writing – original draft (lead). **Petra E. Jönsson:** Conceptualization (supporting); Data curation (equal); Formal analysis (equal); Investigation (equal); Supervision (equal); Visualization (equal); Writing – review & editing (equal). **Sagar Ghorai:** Data curation (supporting); Investigation (equal);

Writing – review & editing (supporting). **Alpha T. N'Diaye**: Data curation (supporting); Formal analysis (supporting); Investigation (equal); Methodology (supporting); Resources (equal). **Gabriella Andersson**: Conceptualization (equal); Funding acquisition (lead); Project administration (lead); Supervision (lead); Writing – review & editing (lead).

DATA AVAILABILITY

The data that support the findings of this study are available from the corresponding author upon reasonable request.

REFERENCES

- 1A. Hirohata, K. Yamada, Y. Nakatani, I.-L. Prejbeanu, B. Diény, P. Pirro, and B. Hillebrands, "Review on spintronics: Principles and device applications," *J. Magn. Magn. Mater.* **509**, 166711 (2020).
- 2J. A. González, J. P. Andrés, and R. López Antón, "Applied trends in magnetic rare earth/transition metal alloys and multilayers," *Sensors* **21**, 5615 (2021).
- 3E. Goto, N. Hayashi, T. Miyashita, and K. Nakagawa, "Magnetization and switching characteristics of composite thin magnetic films," *J. Appl. Phys.* **36**, 2951–2958 (1965).
- 4E. F. Kneller and R. Hawig, "The exchange-spring magnet: A new material principle for permanent magnets," *IEEE Trans. Magn.* **27**, 3588–3560 (1991).
- 5R. Skomski and J. Coey, "Giant energy product in nanostructured two-phase magnets," *Phys. Rev. B* **48**, 15812 (1993).
- 6D. Suess, T. Schrefl, S. Fähler, M. Kirschner, G. Hrkac, F. Dorfbauer, and J. Fidler, "Exchange spring media for perpendicular recording," *Appl. Phys. Lett.* **87**, 012504 (2005).
- 7D. Suess, "Multilayer exchange spring media for magnetic recording," *Appl. Phys. Lett.* **89**, 113105 (2006).
- 8M. Heigl, C. Vogler, A.-O. Mandru, X. Zhao, H. J. Hug, D. Suess, and M. Albrecht, "Microscopic origin of magnetization reversal in nanoscale exchange-coupled ferri/ferromagnetic bilayers: Implications for high energy density permanent magnets and spintronic devices," *ACS Appl. Nano Mater.* **3**, 9218–9225 (2020).
- 9A. Hindmarch, C. Kinane, M. MacKenzie, J. Chapman, M. Henini, D. Taylor, D. Arena, J. Dvorak, B. Hickey, and C. Marrows, "Interface induced uniaxial magnetic anisotropy in amorphous CoFeB films on AlGaAs (001)," *Phys. Rev. Lett.* **100**, 117201 (2008).
- 10F. Magnus, R. Moubah, U. B. Arnalds, V. Kapaklis, A. Brunner, R. Schäfer, G. Andersson, and B. Hjörvarsson, "Giant magnetic domains in amorphous SmCo thin films," *Phys. Rev. B* **89**, 224420 (2014).
- 11F. Magnus, R. Moubah, V. Kapaklis, G. Andersson, and B. Hjörvarsson, "Magnetostrictive properties of amorphous SmCo thin films with imprinted anisotropy," *Phys. Rev. B* **89**, 134414 (2014).
- 12W. Liang, H. Zhou, J. Xiong, F. Hu, J. Li, J. Zhang, J. Wang, J. Sun, and B. Shen, "Tunable in-plane anisotropy in amorphous Sm-Co films grown on (011)-oriented single-crystal substrates," *Engineering* **6**, 159–164 (2020).
- 13H. Raanaei, H. Nguyen, G. Andersson, H. Lidbaum, P. Korelis, K. Leifer, and B. Hjörvarsson, "Imprinting layer specific magnetic anisotropies in amorphous multilayers," *J. Appl. Phys.* **106**, 023918 (2009).
- 14P. Rani, G. Muscas, H. Stopfel, G. Andersson, and P. E. Jönsson, "Rigid exchange coupling in rare-earth-lean amorphous hard/soft nanocomposites," *Adv. Electron. Mater.* **6**, 2000573 (2020).
- 15R. Procter, F. Magnus, G. Andersson, C. Sánchez-Hanke, B. Hjörvarsson, and T. Hase, "Magnetic leverage effects in amorphous SmCo/CoAlZr heterostructures," *Appl. Phys. Lett.* **107**, 062403 (2015).
- 16W. A. Sibley, C. M. Nelson, and Y. Chen, "Luminescence in MgO," *J. Chem. Phys.* **48**, 4582 (1968).
- 17C. Chen, Y. Idzerda, H.-J. Lin, G. Meigs, A. Chaiken, G. Prinz, and G. Ho, "Element-specific magnetic hysteresis as a means for studying heteromagnetic multilayers," *Phys. Rev. B* **48**, 642 (1993).
- 18M. Björck and G. Andersson, "GenX: An extensible X-ray reflectivity refinement program utilizing differential evolution," *J. Appl. Crystallogr.* **40**, 1174–1178 (2007).
- 19H. Zhang, D. Zeng, and Z. Liu, "The law of approach to saturation in ferromagnets originating from the magnetocrystalline anisotropy," *J. Magn. Magn. Mater.* **322**, 2375–2380 (2010).
- 20E. C. Stoner and E. Wohlfarth, "A mechanism of magnetic hysteresis in heterogeneous alloys," *Philos. Trans. R. Soc. London, Ser. A: Math. Phys. Sci.* **240**, 599–642 (1948).
- 21N. Suponev, R. Grechishkin, M. Lyakhova, and Y. E. Pushkar, "Angular dependence of coercive field in (Sm, Zr)(Co, Cu, Fe)₂ alloys," *J. Magn. Magn. Mater.* **157**, 376–377 (1996).
- 22M. Mathews, E. P. Houwman, H. Boschker, G. Rijnders, and D. H. Blank, "Magnetization reversal mechanism in La_{0.67}Sr_{0.33}MnO₃ thin films on NdGaO₃ substrates," *J. Appl. Phys.* **107**, 013904 (2010).
- 23V. Barwal, S. Husain, N. Behera, E. Goyat, and S. Chaudhary, "Growth dependent magnetization reversal in Co₂MnAl full Heusler alloy thin films," *J. Appl. Phys.* **123**, 053901 (2018).
- 24P. Carra, B. Thole, M. Altarelli, and X. Wang, "X-ray circular dichroism and local magnetic fields," *Phys. Rev. Lett.* **70**, 694 (1993).
- 25B. Thole, P. Carra, F. Sette, and G. van der Laan, "X-ray circular dichroism as a probe of orbital magnetization," *Phys. Rev. Lett.* **68**, 1943 (1992).
- 26C. Chen, Y. Idzerda, H.-J. Lin, N. Smith, G. Meigs, E. Chaban, G. Ho, E. Pellegrin, and F. Sette, "Experimental confirmation of the x-ray magnetic circular dichroism sum rules for iron and cobalt," *Phys. Rev. Lett.* **75**, 152 (1995).
- 27S. Kanai, M. Tsujikawa, Y. Miura, M. Shirai, F. Matsukura, and H. Ohno, "Magnetic anisotropy in Ta/CoFeB/MgO investigated by x-ray magnetic circular dichroism and first-principles calculation," *Appl. Phys. Lett.* **105**, 222409 (2014).
- 28R. Wu and A. J. Freeman, "Limitation of the magnetic-circular-dichroism spin sum rule for transition metals and importance of the magnetic dipole term," *Phys. Rev. Lett.* **73**, 1994–1997 (1994).
- 29A. Frisk, M. Ahlberg, G. Muscas, S. George, R. Johansson, W. Klysubun, P. E. Jönsson, and G. Andersson, "Magnetic and structural characterization of CoFeZr thin films grown by combinatorial sputtering," *Phys. Rev. Mater.* **3**, 074403 (2019).
- 30H. Adachi and H. Ino, "A ferromagnet having no net magnetic moment," *Nature* **401**, 148–150 (1999).
- 31S. S. Dhesi, P. Bencok, N. B. Brookes, G. van der Laan, and R. M. Galéra, "X-ray magnetic circular dichroism study of SmAl₂ using the M_{4,5} x-ray absorption edges," *J. Appl. Phys.* **93**, 8337–8339 (2003).
- 32S. S. Dhesi, G. van der Laan, P. Bencok, N. B. Brookes, R. M. Galéra, and P. Ohresser, "Spin- and orbital-moment compensation in the zero-moment ferromagnet Sm_{0.974}Gd_{0.026}Al₂," *Phys. Rev. B* **82**, 180402 (2010).